

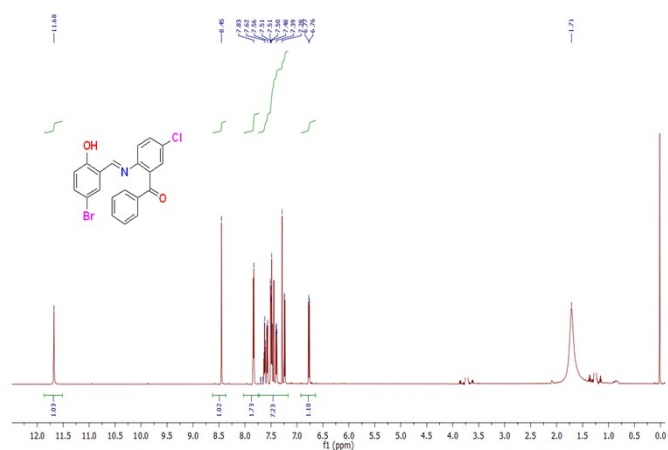
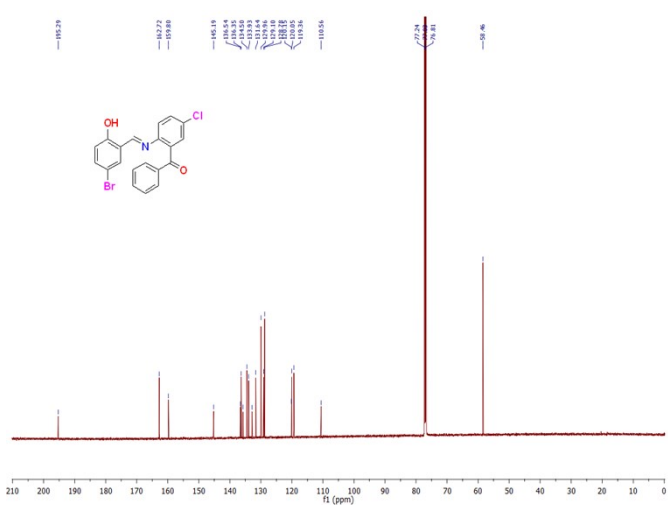
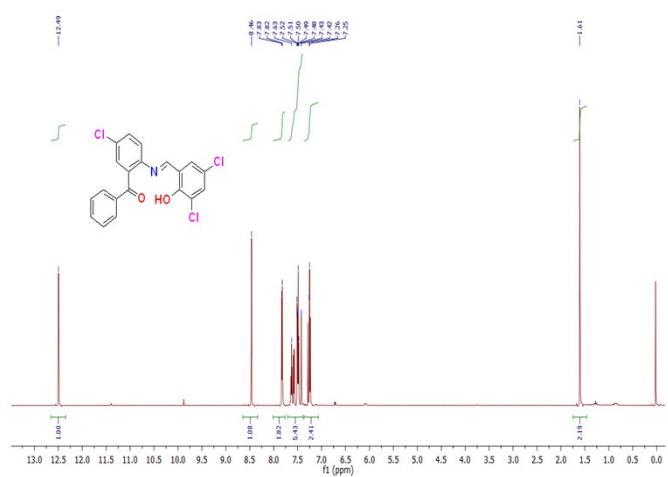
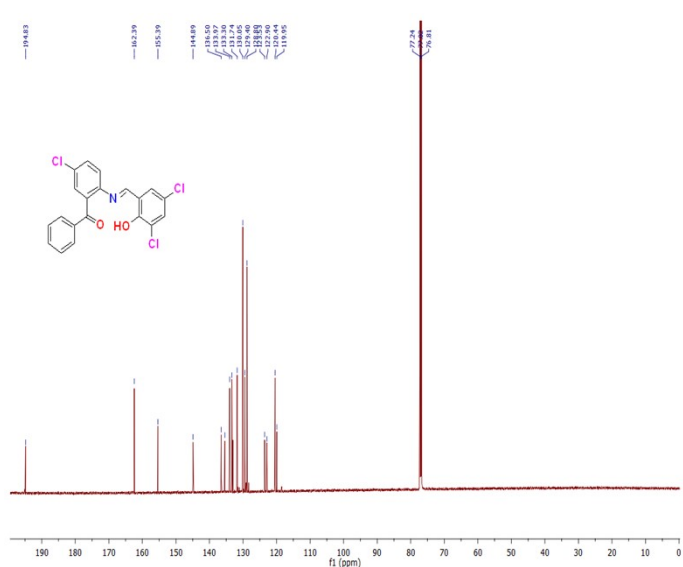
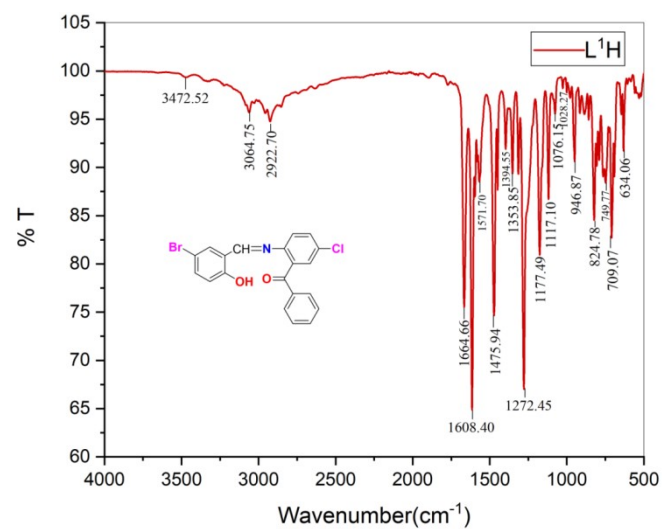
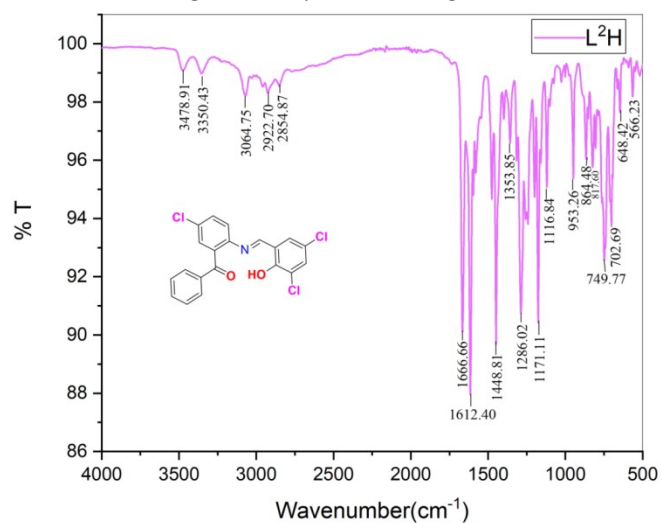
ARTICLE

**Supporting Information for
Synthesis and characterization of novel copper (II) complexes as
potential drug candidates against SARS CoV-2 main protease**

Sunil Kumar^a, and Mukesh Choudhary^{a*}

^a Department of Chemistry, National Institute of Technology Patna, Patna-800005
(Bihar) India.

^{a,*}Corresponding author: mukesh@nitp.ac.in

Figure S1. $^1\text{H-NMR}$ spectra of L^1H ligand.Figure S2. $^{13}\text{C-NMR}$ spectra of L^1H ligand.Figure S3. $^1\text{H-NMR}$ spectra of L^2H ligand.Figure S4. $^{13}\text{C-NMR}$ spectra of L^2H ligand.Figure S5. IR spectra of L^1H ligand.Figure S6. IR spectra of L^2H ligand.

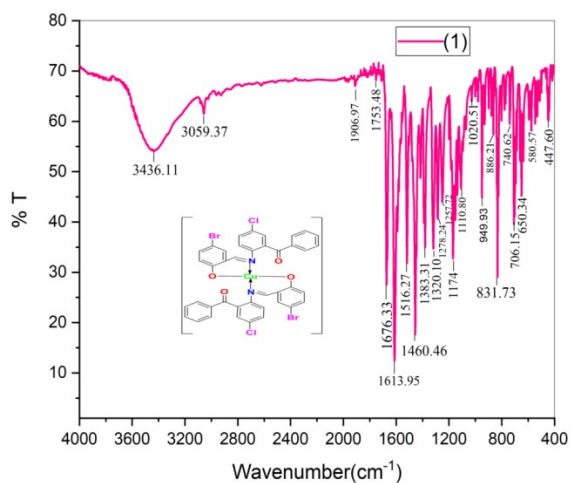
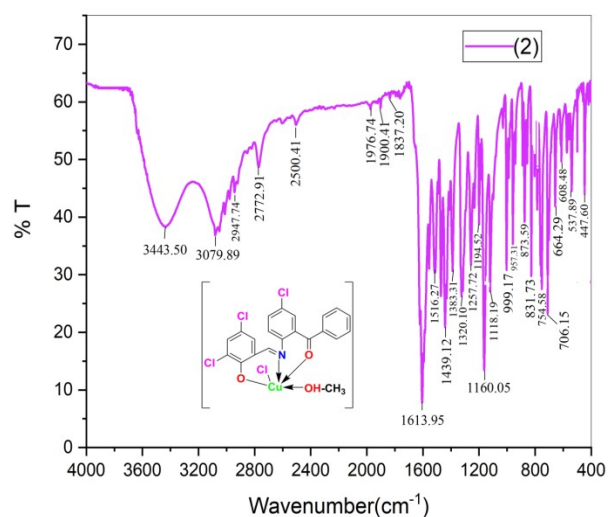


Figure S7. IR spectrum of copper(II) Schiff base complex $[\text{Cu}(\text{L}^1)_2](1)$.



S8. IR spectrum of copper(II) Schiff base complex $[\text{Cu}(\text{L}^2)(\text{CH}_3\text{OH})(\text{Cl})](2)$.

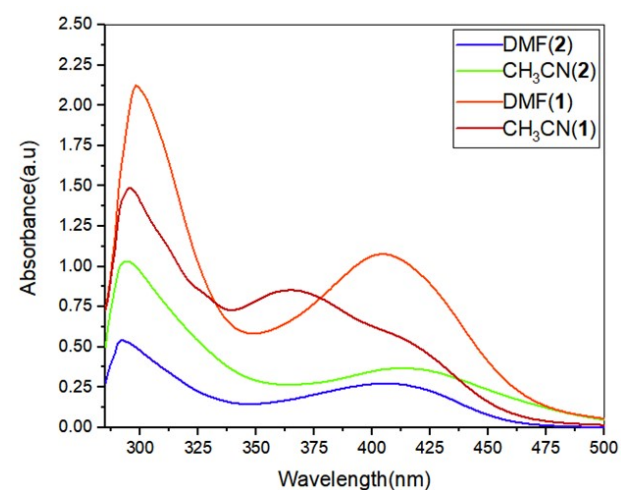
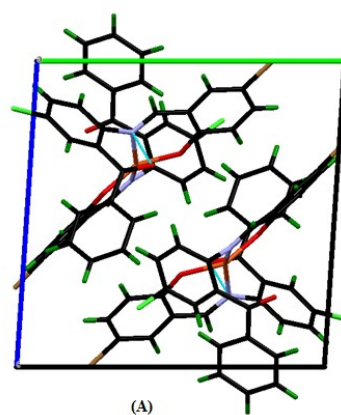
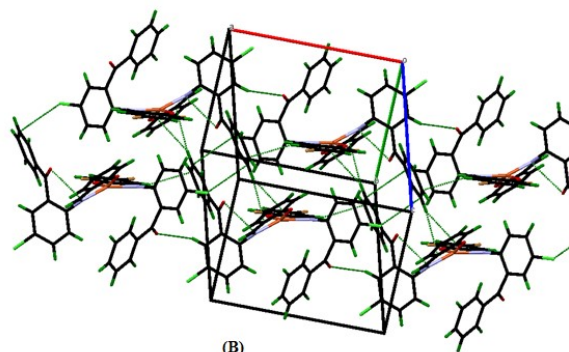


Figure S9. Electronic spectra ($1 \times 10^{-3} \text{M}$) of copper (II) Schiff base complex $[\text{Cu}(\text{L}^1)_2](1)$ and $[\text{Cu}(\text{L}^2)(\text{CH}_3\text{OH})(\text{Cl})](2)$.



(A)



(B)

Figure S10. A packing views (A & B) of copper (II) complex $[\text{Cu}(\text{L}^1)_2](1)$ (along the a-axis).

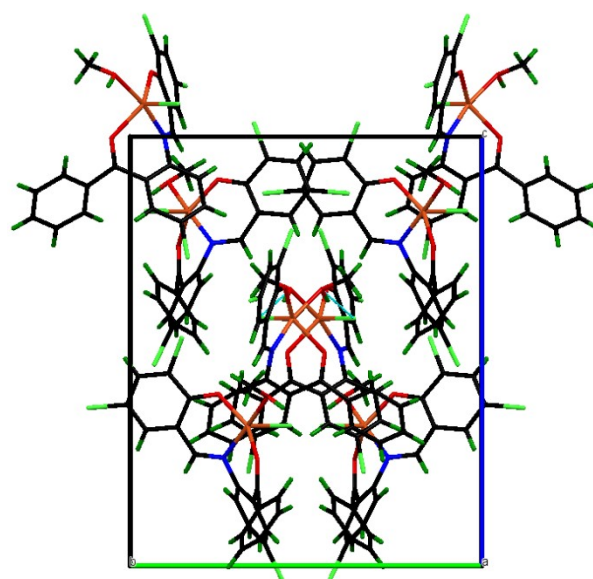


Figure S11. A packing view of copper (II) complex $[\text{Cu}(\text{L}^2)(\text{CH}_3\text{OH})(\text{Cl})](2)$ (along the a-axis).

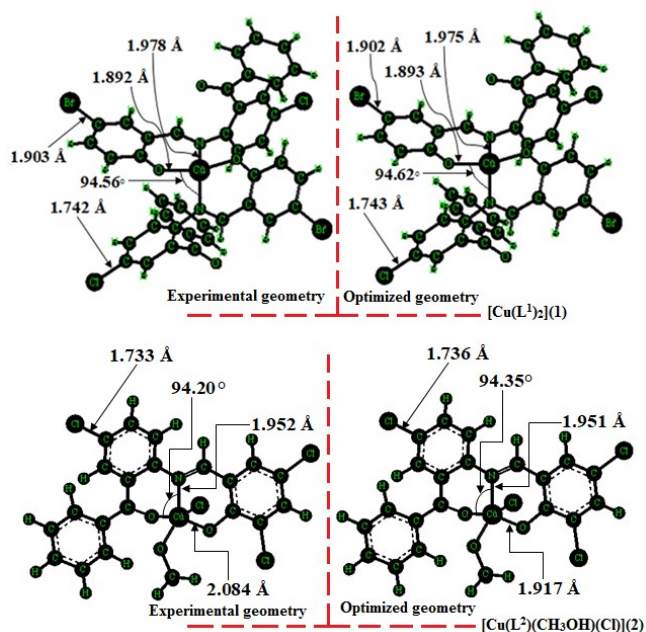


Figure S12. Experimental and optimized geometry of copper (II) complex $[Cu(L^1)_2](1)$ and $[Cu(L^2)(CH_3OH)(Cl)](2)$.

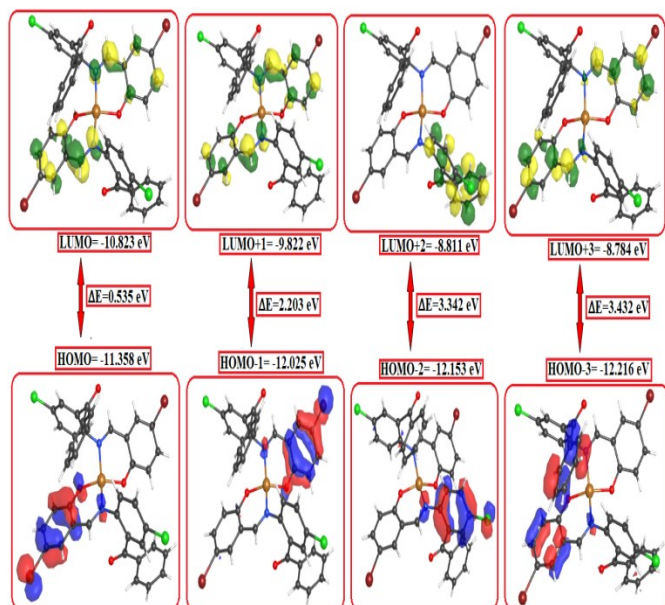


Figure S13. Frontier molecular orbitals of copper (II) Schiff base complex $[Cu(L^1)_2](1)$.

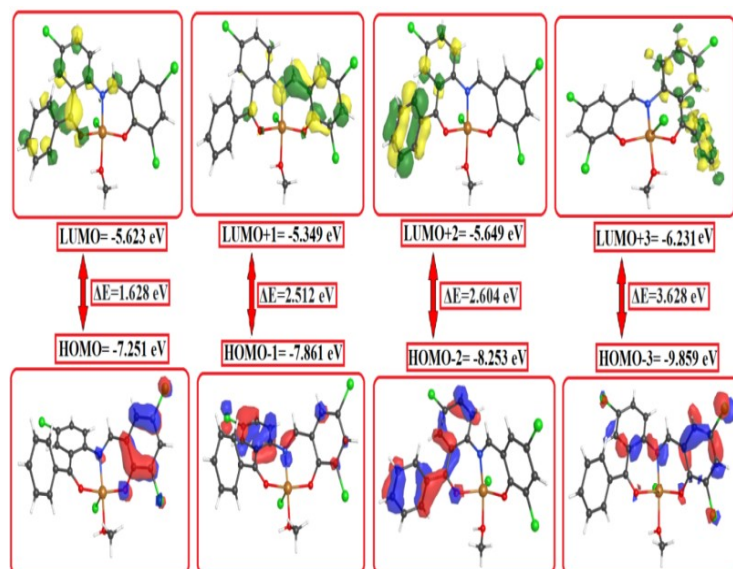


Figure S14. Frontier molecular orbital diagram of copper (II) complex $[Cu(L^2)(CH_3OH)(Cl)](2)$.

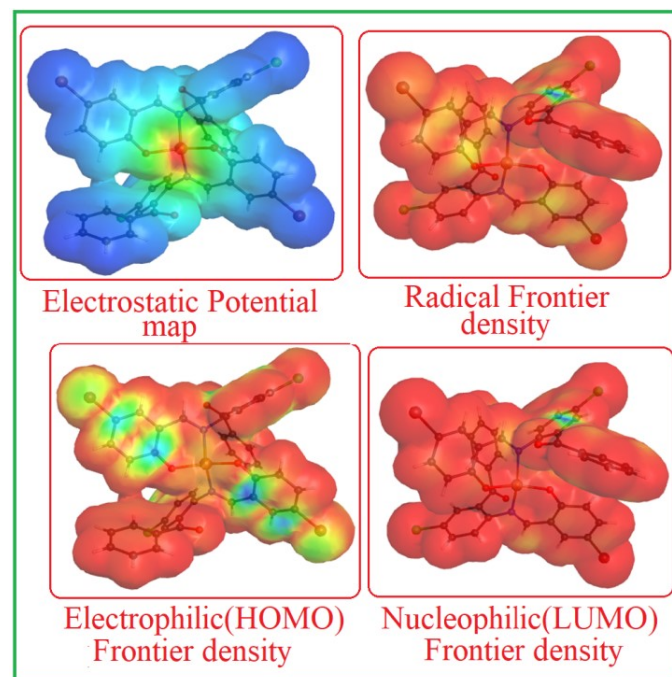


Figure S15. Electrostatic potential maps of copper (II) Schiff base complex $[Cu(L^1)_2](1)$.

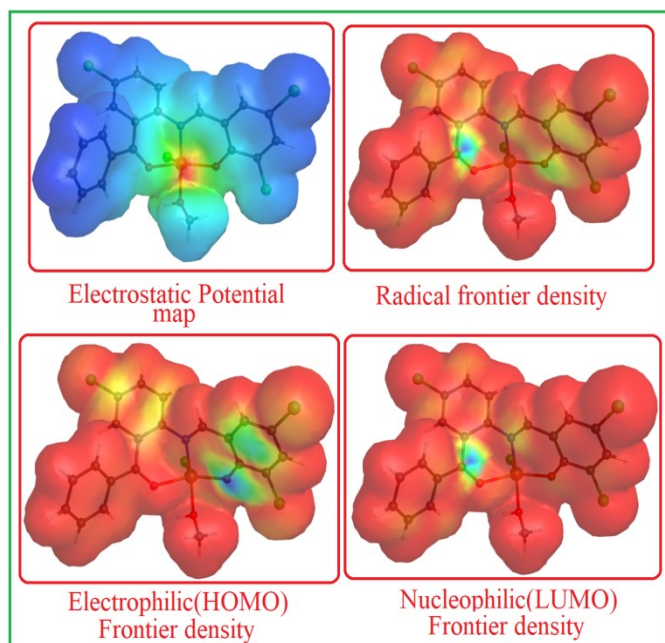


Figure S16. Electrostatic potential maps of copper (II) Schiff base complex $[\text{Cu}(\text{L}^2)(\text{CH}_3\text{OH})(\text{Cl})](2)$.

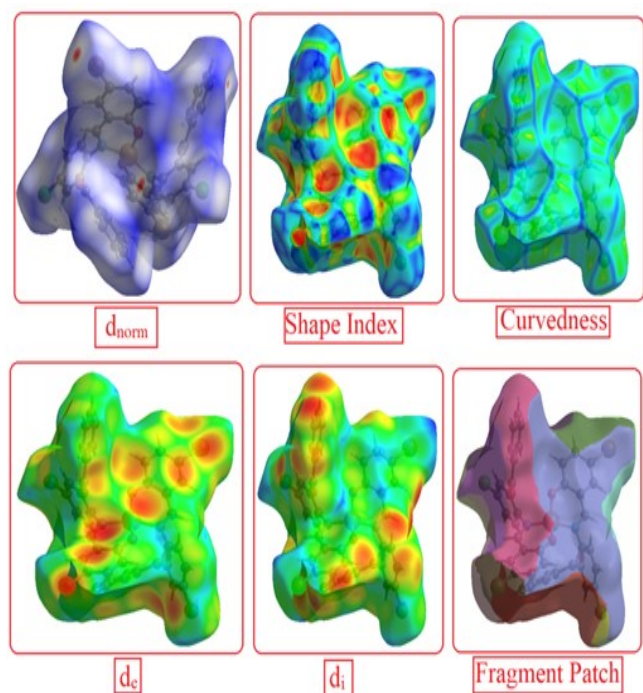


Figure S17. Graphical view of the Hirshfeld surfaces (full portion) mapped with d_{norm} property; red spots represents the closest contacts and blue color the most distant contacts for copper (II) Schiff base complex $[\text{Cu}(\text{L}^1)_2](1)$.

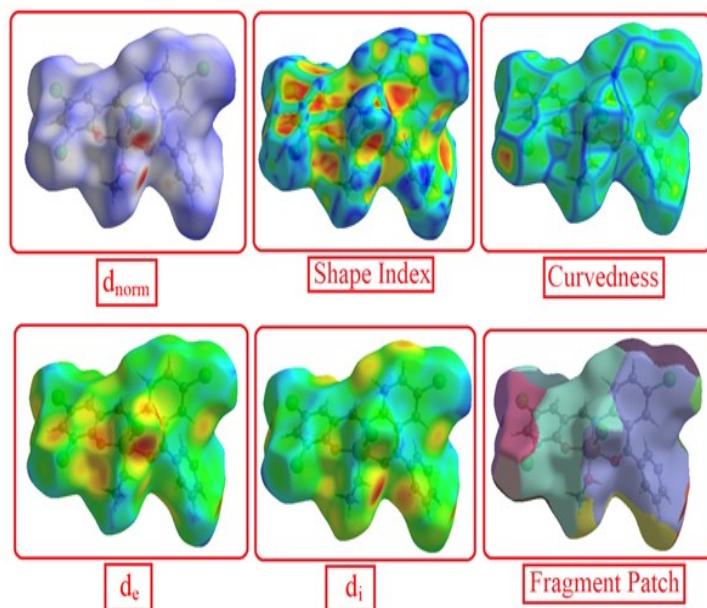


Figure S18. Graphical view of the Hirshfeld surfaces (full portion) mapped with d_{norm} property; red spots represents the closest contacts and blue color the most distant contacts for copper (II) Schiff base complex $[\text{Cu}(\text{L}^2)(\text{CH}_3\text{OH})(\text{Cl})](2)$.

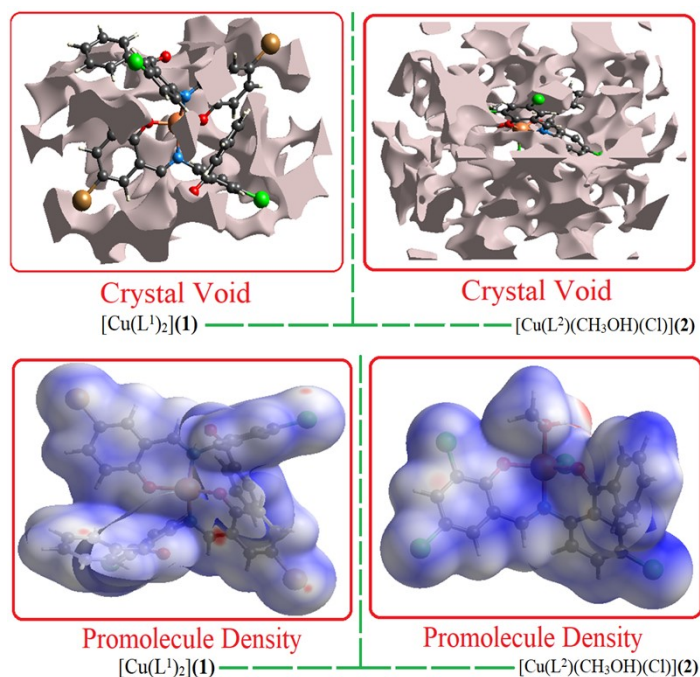


Figure S19. Crystal void and promolecule density surface of copper (II) Schiff base complex $[\text{Cu}(\text{L}^1)_2](1)$ and $[\text{Cu}(\text{L}^2)(\text{CH}_3\text{OH})(\text{Cl})](2)$.

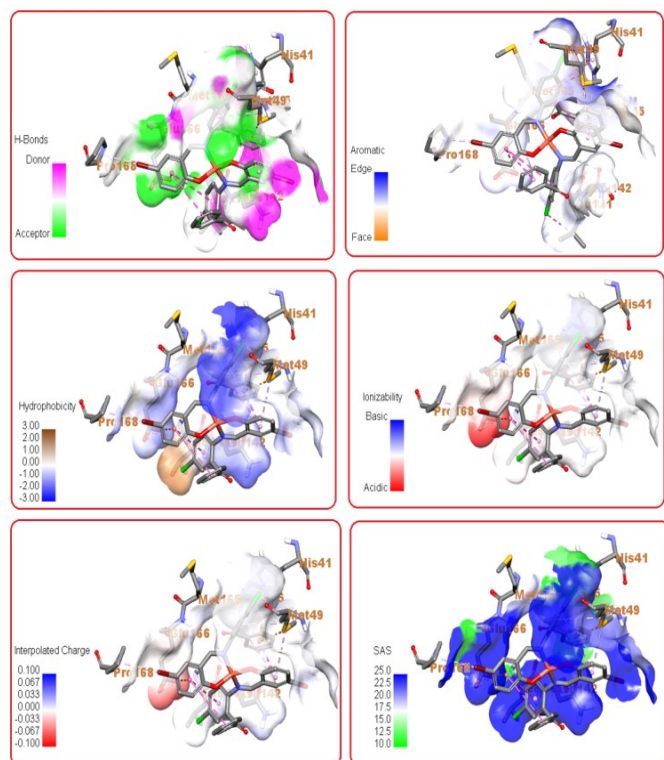


Figure S20. The representation of docked copper (II) complex $[\text{Cu}(\text{L}^1)_2](1)$ inside the MPr^{O} protein (PDB ID: 7BRP) with its focused view for interacting residues along with H bond and intermolecular interactions; (a) H-bond donor and acceptor meshes represented by pink and light green colours, respectively; (b) Aromatic receptor surface represented by blue(Edge) and orange(face) colours; (c) Hydrophobic pocket represented with blue and brown colours; (d) ionizability receptor surface represented by blue (basic) and red (acidic) colours; (e) interpolated charge receptor surface represented by blue and red colours; (f) SAS receptor surface represented by blue and green colours, respectively.

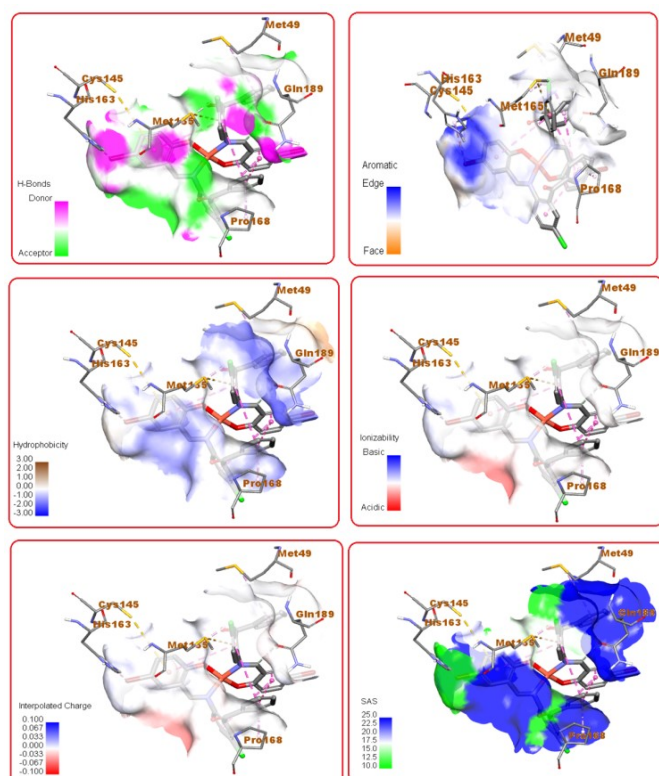


Figure S21. The representation of docked copper (II) complex $[\text{Cu}(\text{L}^1)_2](1)$ inside the MPr^{O} protein (PDB ID: 7BUY) with its focused view for interacting residues along with H-bond and intermolecular interactions; (a) H-bond donor and acceptor meshes represented by pink and light green colours, respectively; (b) Aromatic receptor surface represented by blue(Edge) and orange (face) colours; (c) Hydrophobic pocket represented with blue and brown colours; (d) ionizability receptor surface represented by blue (basic) and red (acidic) colours; (e) interpolated charge receptor surface represented by blue and red colours; (f) SAS receptor surface represented by blue and light green colours, respectively.

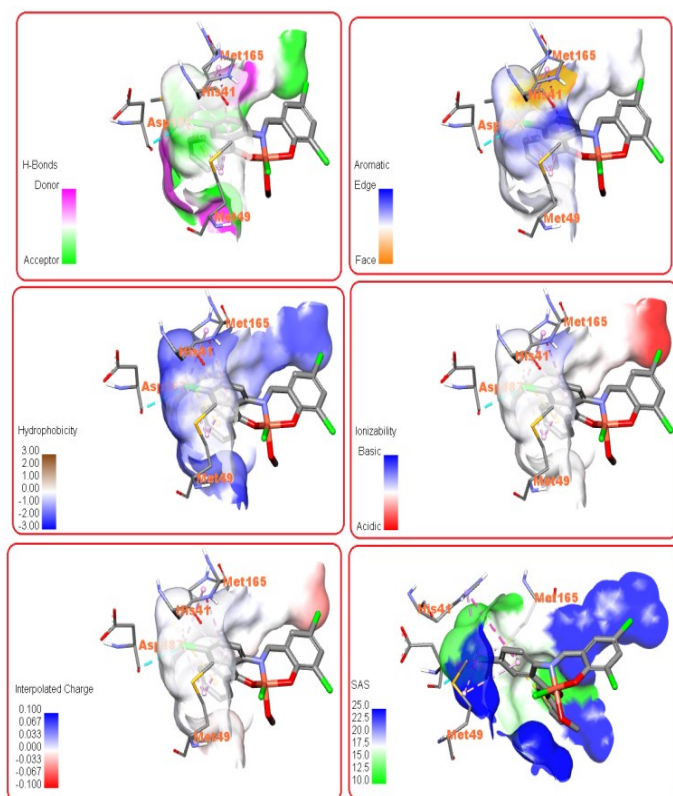


Figure S22. The representation of docked copper (II) complex $[\text{Cu}(\text{L}^2)(\text{CH}_3\text{OH})(\text{Cl})](2)$ inside the M^{PRO} protein (PDB ID: 7BUY) with its focused view for interacting residues along with H bond and intermolecular interactions; (a) H-bond donor and acceptor meshes represented by pink and light green colors, respectively; (b) Aromatic receptor surface represented by blue(Edge) and orange(face) colours; (c) Hydrophobic pocket represented with blue and brown colours; (d) ionizability receptor surface represented by blue (basic) and red (acidic) colours; (e) interpolated charge receptor surface represented by blue and red colours; (f) SAS receptor surface represented by blue and light green colours, respectively.

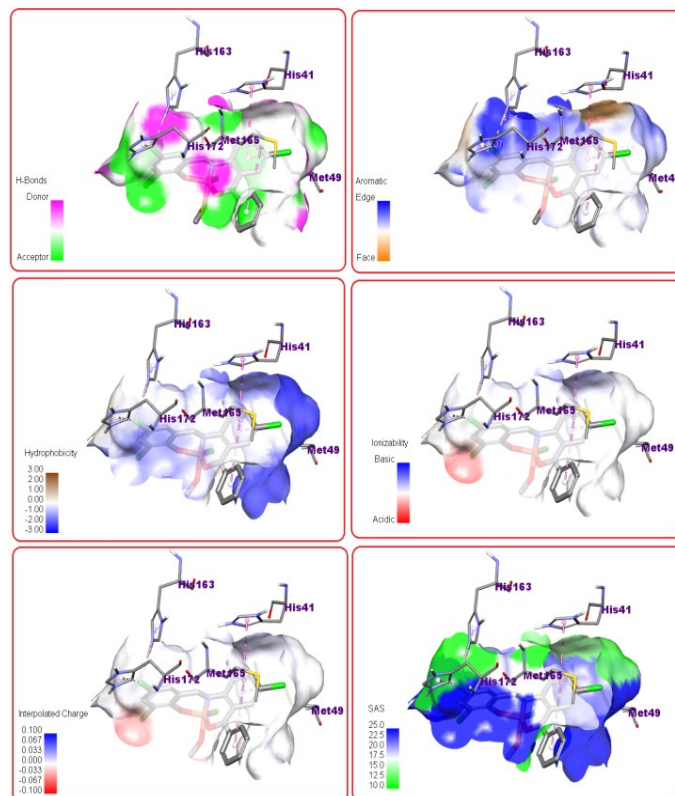


Figure S23. The representation of docked copper (II) complex $[\text{Cu}(\text{L}^2)(\text{CH}_3\text{OH})(\text{Cl})](2)$ inside the M^{PRO} protein (PDB ID: 7BRP) with its focused view for interacting residues along with H bond and intermolecular interactions; (a) H-bond donor and acceptor meshes represented by pink and light green colours, respectively; (b) Aromatic receptor surface represented by blue(Edge) and orange(face) colours; (c) Hydrophobic pocket represented with blue and brown colours; (d) ionizability receptor surface represented by blue (basic) and red (acidic) colours; (e) interpolated charge receptor surface represented by blue and red colours; (f) SAS receptor surface represented by blue and light green colours, respectively.

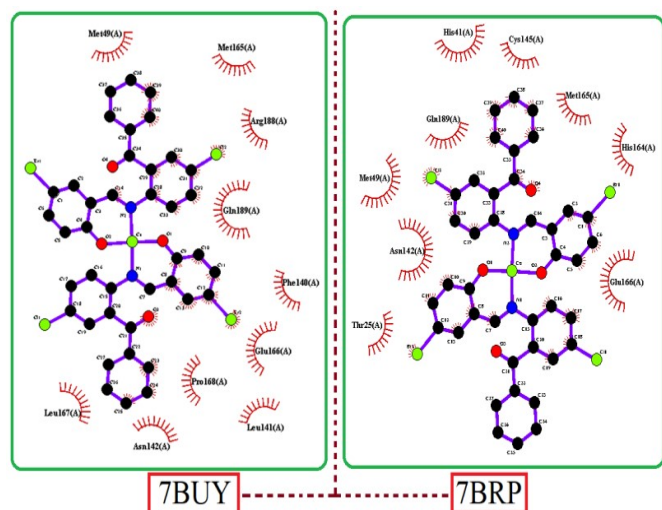


Figure S24. Two-dimensional Lig-plot image of complex $[\text{Cu}(\text{L}^1)_2]$ (**1**) with SARS-CoV-2 main protease (M^{pro} - 7BUY and 7BRP).

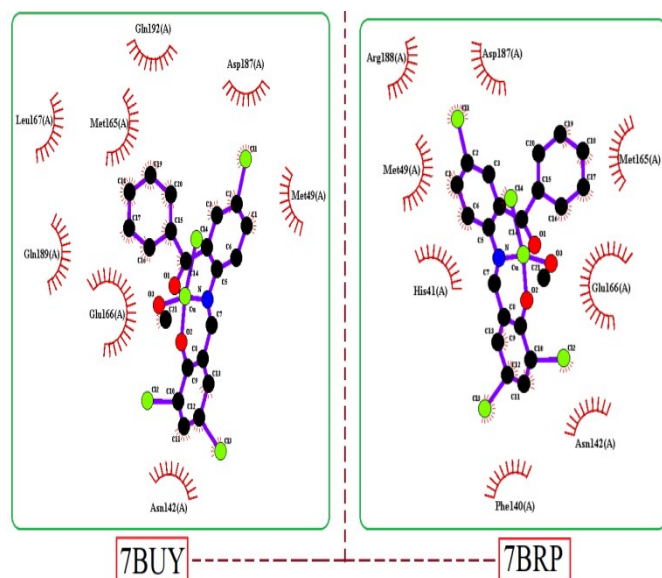


Figure S25. Two-dimensional Lig-plot image of the complex $[\text{Cu}(\text{L}^2)(\text{CH}_3\text{OH})(\text{Cl})]$ (**2**) with SARS-CoV-2 main protease (M^{pro} - 7BUY and 7BRP).

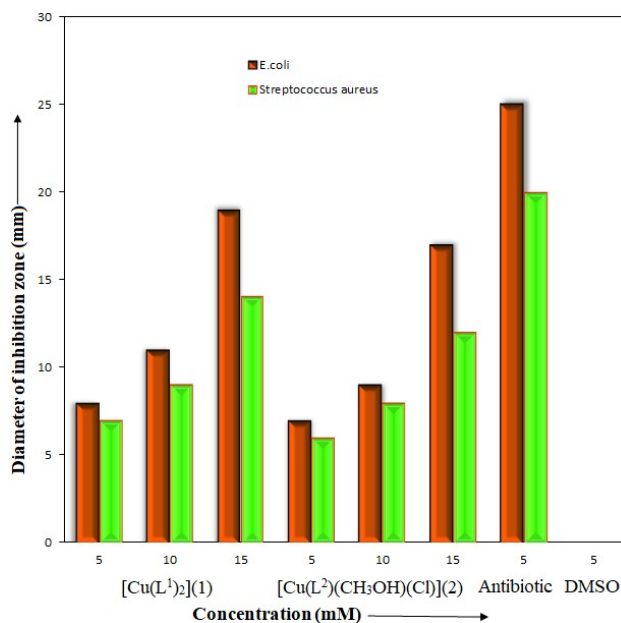


Figure S26. Graphical representation of antibacterial activity for the copper (II) Schiff base complex $[\text{Cu}(\text{L}^1)_2]$ (**1**) and $[\text{Cu}(\text{L}^2)(\text{CH}_3\text{OH})(\text{Cl})]$ (**2**).

Table S1. Hydrogen bonds for copper (II) Schiff base complex $[\text{Cu}(\text{L}^1)_2]$ (**1**) and $[\text{Cu}(\text{L}^2)(\text{CH}_3\text{OH})(\text{Cl})]$ (**2**) [Å and °].

D-H...A	d(D-H)	d(H...A)	d(D...A)	<(DHA)
(1)				
C(11)-H(11)...Br(1)#1	0.95	3.02	3.851(3)	147.0
C(29)-H(29)...Br(1)#2	0.95	3.07	3.960(3)	157.2
(2)				
C(14)-H(14)...O(2)#1	0.95	2.52	3.424(9)	158.1
O(3)-H(3A)...Cl(4)#2	0.84	2.20	3.018(5)	163.3

Symmetry transformations used to generate equivalent atoms:

#1 $-x+1, -y+1, -z+2$ #2 $x, y+1, z$ for (**1**);

#1 $y-1/2, -x+1, z-1/4$ #2 $-x+1, -y+1, z$ for (**2**)

Table S2. The computed values of E_{HOMO} , E_{LUMO} and energy gap ($E_{\text{LUMO}} - E_{\text{HOMO}}$)^a for complex $[\text{Cu}(\text{L}^1)_2](\mathbf{1})$ and $[\text{Cu}(\text{L}^2)(\text{CH}_3\text{OH})(\text{Cl})](\mathbf{2})$.

	(1)	(2)
E_{HOMO}	-11.358	-7.251
E_{LUMO}	-10.823	-5.623
ΔE	0.535	1.628
$E_{\text{HOMO}-1}$	-12.025	-7.861
$E_{\text{LUMO}+1}$	-9.822	-5.349
ΔE	2.203	2.512
$E_{\text{HOMO}-2}$	-12.153	-8.253
$E_{\text{LUMO}+2}$	-8.811	-5.649
ΔE	3.342	2.604

^a Energy gap (ΔE) = $E_{\text{LUMO}} - E_{\text{HOMO}}$; units in eV.

Table S3. Computed values for Global reactivity descriptors of the studied complex $[\text{Cu}(\text{L}^1)_2](\mathbf{1})$ and $[\text{Cu}(\text{L}^2)(\text{CH}_3\text{OH})(\text{Cl})](\mathbf{2})$.

	(1)	(2)
IP	11.358	7.251
EA	10.823	5.623
χ	11.091	6.437
η	0.634	0.407
μ	-11.091	-6.437
ω	97.011	50.903
σ	0.789	1.229

IP= ionization potential, EA= electron affinity, χ = electro negativity, μ =chemical potential, η = global hardness, σ =global softness and ω = global electrophilicity; units in eV.

Table S4. Interaction energies for complex $[\text{Cu}(\text{L}^1)_2](\mathbf{1})$ calculated with CE-B3LYP model. It can be seen from the interaction energies that the hydrogen bonding motif between the central molecules (highlighted in yellow mesh) and the $-x +1/2, y +1/2, z +1/2$ symmetry-related molecule (line green) is by far the strongest interaction among near neighbours, with interaction energy of $-41.2 \text{ kJ mol}^{-1}$.

Complex $[\text{Cu}(\text{L}^1)_2](\mathbf{1})$									
	N	Symop	R	Electron Density	E_ele	E_pol	E_dis	E_rep	E_tot
	2	x, y, z	11.18	HF/3-21G	-11.9	-4.2	-52.6	23.0	-43.7
	1	-x, -y, -z	6.96	HF/3-21G	-27.7	-10.1	-111.7	52.3	-93.0
	2	x, y, z	12.55	HF/3-21G	0.0	-1.1	0.0	0.0	-0.7
	1	-x, -y, -z	10.07	HF/3-21G	-23.0	-6.6	-112.3	65.8	-75.5
	2	x, y, z	12.54	HF/3-21G	0.0	-0.9	0.0	0.0	-0.6
	1	-x, -y, -z	10.54	HF/3-21G	-16.7	-5.5	-57.0	30.6	-47.1
	1	-x, -y, -z	12.26	HF/3-21G	0.0	-3.2	0.0	0.0	-2.1
	1	-x, -y, -z	10.25	HF/3-21G	-20.5	-5.2	-95.5	58.7	-62.7
	1	-x, -y, -z	11.49	HF/3-21G	-7.3	-2.5	-44.1	21.3	-31.5
	1	-x, -y, -z	12.35	HF/3-21G	0.0	-1.9	0.0	0.0	-1.3
	1	-x, -y, -z	11.81	HF/3-21G	-1.6	-2.3	-15.2	5.1	-12.7
Energy Model					k_ele	k_pol	k_disp	k_rep	
CE-HF ... HF/3-21G electron densities					1.019	0.651	0.901	0.811	
CE-B3LYP ... B3LYP/6-31G(d,p) electron densities					1.057	0.740	0.871	0.618	

Table S5. Interaction energies for complex $[\text{Cu}(\text{L}^2)(\text{CH}_3\text{OH})(\text{Cl})](\mathbf{2})$ calculated with CE-B3LYP model. It can be seen from the interaction energies table that the hydrogen bonding motif between the central molecules (highlighted in yellow mesh) and the $-x +1/2, y +1/2, z +1/2$ symmetry-related molecule (line green) is by far the strongest interaction among near neighbors, with interaction energy of $-44.6 \text{ kJ mol}^{-1}$.

Complex $[\text{Cu}(\text{L}^2)(\text{CH}_3\text{OH})(\text{Cl})](\mathbf{2})$									
	N	Symop	R	Electron Density	E_ele	E_pol	E_dis	E_rep	E_tot
	1	-x, -y, z	8.45	HF/3-21G	-8.4	-2.6	-47.3	25.3	-32.3
	2	x+1/2, y+1/2, z+1/2	14.30	HF/3-21G	0.0	-1.8	0.0	0.0	-1.2
	2	-y, x+1/2, z+1/4	13.78	HF/3-21G	0.0	-0.5	0.0	0.0	-0.3
	2	y+1/2, -x, z+3/4	6.51	HF/3-21G	-60.7	-38.0	-67.9	46.0	-110.4
	2	-x+1/2, -y+1/2, z+1/2	12.95	HF/3-21G	0.0	-1.9	0.0	0.0	-1.2
	1	-x, -y, z	7.08	HF/3-21G	-183.6	-71.7	-76.0	150.3	-180.3
	2	-y, x+1/2, z+1/4	14.73	HF/3-21G	0.0	-0.4	0.0	0.0	-0.2
	2	-x+1/2, -y+1/2, z+1/2	11.34	HF/3-21G	-12.9	-2.1	-14.1	6.9	-21.6
	2	-y+1/2, x, z+3/4	7.87	HF/3-21G	8.6	-6.2	-33.2	13.5	-14.2
Energy Model					k_ele	k_pol	k_disp	k_rep	
CE-HF ... HF/3-21G electron densities					1.019	0.651	0.901	0.811	
CE-B3LYP ... B3LYP/6-31G(d,p) electron densities					1.057	0.740	0.871	0.618	

Table S6. The structure activity relationship established between the structures and their potential applications against SARS-CoV-2 main protease(M^{Pro}) of the copper complex(II) [Cu(L¹)₂](**1**) and [Cu(L²)(CH₃OH)(Cl)] (**2**).

Complexes		Experimental bond lengths (Å)		Docked complex inside SARS-CoV-2 bond lengths (Å)	
(1)	7BUY	Cu(1)-O(1)	1.8926	Cu(1)-O(1)	1.8931
		Cu(1)-O(3)	1.8898	Cu(1)-O(3)	1.8902
		Cu(1)-N(1)	1.9738	Cu(1)-N(1)	1.9751
		Cu(1)-N(2)	1.9784	Cu(1)-N(2)	1.9772
	7BRP	Cu(1)-O(1)	1.8926	Cu(1)-O(1)	1.8927
		Cu(1)-O(3)	1.8898	Cu(1)-O(3)	1.8899
		Cu(1)-N(1)	1.9738	Cu(1)-N(1)	1.9732
		Cu(1)-N(2)	1.9784	Cu(1)-N(2)	1.9779
(2)	7BUY	Cu(1)-O(1)	2.084	Cu(1)-O(1)	2.016
		Cu(1)-O(2)	1.917	Cu(1)-O(2)	1.918
		Cu(1)-O(3)	1.993	Cu(1)-O(3)	1.994
		Cu(1)-N(1)	1.952	Cu(1)-N(1)	1.954
	7BRP	Cu(1)-O(1)	2.084	Cu(1)-O(1)	2.082
		Cu(1)-O(2)	1.917	Cu(1)-O(2)	1.915
		Cu(1)-O(3)	1.993	Cu(1)-O(3)	1.995
		Cu(1)-N(1)	1.952	Cu(1)-N(1)	1.954

Table S7. Antibacterial screening activity of the copper(II) complex [Cu(L¹)₂](**1**) and [Cu(L²)(CH₃OH)(Cl)] (**2**).

Complexes (mM)	Diameter of inhibition zone (in mm)	
	<i>E. coli</i>	<i>S. aureus</i>
(1)		
5	8	7
10	11	9
15	19	14
(2)		
5	7	6
10	9	8
15	17	12
Antibiotic		
5	25	20
DMSO		
5	0	0

Note: Key to interpretation (5-15mM): less than 8 mm, inactive; 9-13 mm, moderately active; above 14 mm, highly active. DMSO (control) shows not clear inhibition zone. Each value is observed within the estimated error limits of ±1 mM.